

## Response to the Comments of Reviewer #2

Comment1(C1): The paper applies a sort of regression analysis to the wintertime (JF) sea ice loss in the Barents-Kara seas. The review of prior literature on Arctic amplification and sea ice loss is often confusing, including in the definition of key concepts such as Arctic amplification or albedo feedback.

Response1(R1): Reviewer #2's comments are difficult to address because of the lack of detail in the review. More specificity is needed so that we can address the concerns of the reviewer. Which parts of the manuscript are confusing in terms of Arctic amplification and sea ice loss? What about the definition of Arctic amplification and albedo feedback is confusing? Arctic amplification represents a rapid warming of the Arctic temperature, the physical interpretation of which may vary from one group of scientists to another. Albedo feedback is a feedback produced by albedo change. In summer, sea ice reduction decreases surface albedo in the Arctic Ocean, thereby increasing the absorption of solar energy in the ocean. This is referred to as albedo feedback in the manuscript.

C2: Based on the explanations given in the manuscript, I cannot understand the authors' methodology sufficiently to judge its value. The manuscript lacks a critical appreciation of the method, e.g. a discussion of how much of the time series and trend is actually captured by the first 'mode' obtained in the analysis.

R2: The methodology was published 20 years ago and has been used in many papers. We cannot repeat the full discussion on the methodology every time a paper is submitted. That is why three key references on the methodology have been added. We tried to improve the method section by including more specific details. [P3 L18-23: ... its amplitude varies from one year to another according to the corresponding PC time series. CSEOF loading vectors are mutually orthogonal to each other in space and time and represent distinct physical processes. The principal component (PC) time series,  $T_n(t)$  are uncorrelated with (and are often nearly independent of) each other. Thus, each loading vector depicts a temporal evolution of spatial patterns seen in a physical process (such as El Niño or seasonal cycle), and corresponding PC time series describes a long-term modulation of the amplitude of the physical process.] [P4 L14-15: A rigorous mathematical explanation of the regression analysis in CSEOF space can be found in Kim et al. (2015).]

We also added how much of the total variability is explained by the sea ice loss mode. As can be seen in Fig. R1, the trend of sea ice reduction is most conspicuous in the Barents-Kara Seas. Figure R1a is very similar to Fig. 1a in the manuscript. Figure R1b also shows that sea ice reduction in the Barents-Kara Seas (red-boxed area in Fig. R1a) is well explained by the sea ice loss mode (red curve).

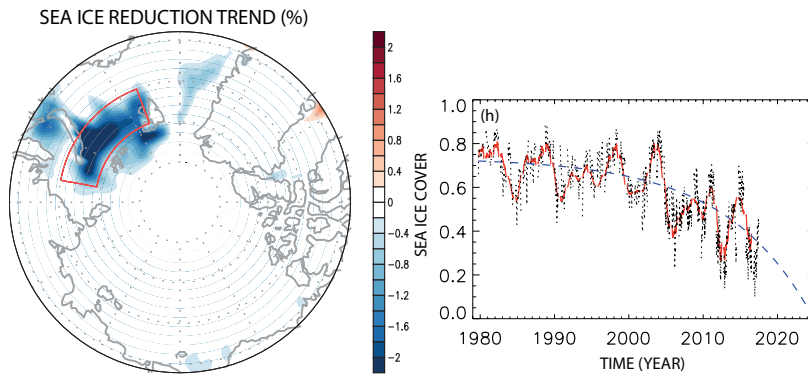


Figure R1. The sea ice trend (% per year) in the Arctic Ocean (left panel) and the sea ice concentration in the red-boxed area of the Barents-Kara Seas (right panel).

5

We made the following change in the revised manuscript: [P4 L17-18: Aside from the winter seasonal cycle, the first CSEOF mode derived from the daily winter sea ice concentration data depicts sea ice loss and associated Arctic warming in the Barents and Kara Sea. This mode explains 24% of the total variability of the sea ice concentration in the Arctic Ocean and is the focus of investigation in the present study.] [P4 L23-26... 37 years (Fig. 1h). The pattern of sea ice reduction (Fig. 1a) is nearly identical with the trend pattern of sea ice concentration in the Arctic Ocean (see Fig. S1 in the supplementary information). As can be seen in Fig. 1h, the sea ice reduction trend in the Barents and Kara Seas (boxed area in Fig. 1a) is faithfully captured by this mode.]

10

C3: My fundamental concern with the manuscript is that it uses correlations to establish causalities and feedbacks, with little regard to the physical and meteorological phenomena discussed. As an example, the feedback loop suggested as a key result of the paper begins with sea ice reduction which supposedly causes warming of 850 hPa temperatures. The alternative explanation that warm air advection contributes to sea ice loss is at least as plausible, but not even mentioned in the manuscript.

15

R3: As we discussed in the “method of analysis” section, the CSEOF technique writes the space-time data in the form

20

$$T(r, t) = \sum_n B_n(r, t) T_n(t), \quad (1)$$

where  $B_n(r, t)$  represents the deterministic (physical) evolution associated with the  $n$ th CSEOF mode and  $T_n(t)$  is the corresponding stochastic amplitude time series. Unlike EOF loading vectors, each CSEOF loading vector is time dependent

and depicts physical (deterministic) evolution. In order to obtain physically consistent loading vectors from different variables, we used regression analysis in CSEOF space, the procedure of which is delineated in the manuscript. After regression analysis in CSEOF space, the entire dataset can be written as

$$Data(r, t) = \sum_n \{B_n(r, t), Z_n(r, t), U_n(r, t), \dots\} T_n(t), \quad (2)$$

5 where the terms in curly braces represent loading vectors from different variables. They are consistent in a physical sense.

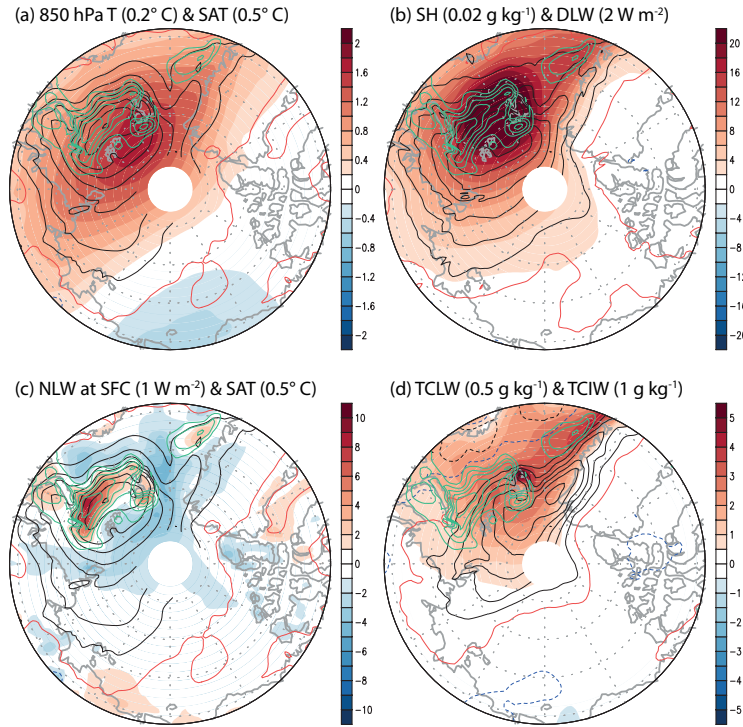


Figure R2. The winter (DJF) averaged regressed patterns of several physical variables (reproduced from Fig. 4 in the manuscript). The caption of each panel shows the shading (contour) interval for the first (second) variable. The red contour is at the first contour level (contour value is identical with the contour interval).

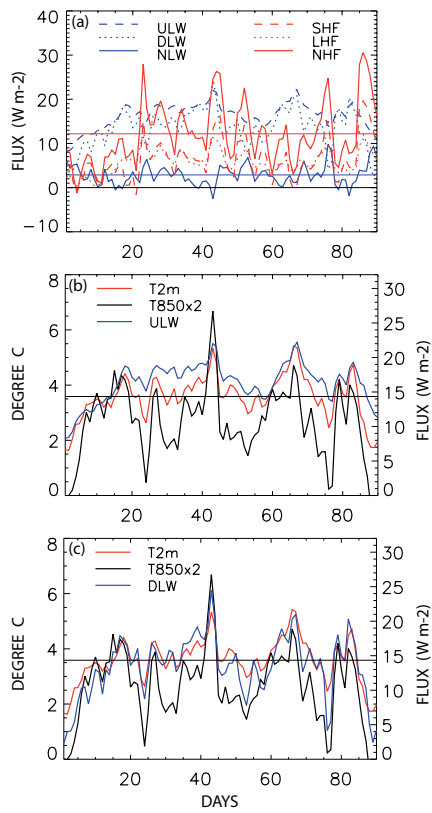


Figure R3. The daily patterns of variability over the region of sea ice loss ( $21^{\circ}$ - $79.5^{\circ}$  E  $\times$   $75^{\circ}$ - $79.5^{\circ}$  N) (reproduced from Figure 6 in the manuscript).

- 5 Our statements are not solely based on correlations. At the very outset, we stated clearly that we would make a quantitative estimate of individual processes involved in an accelerated loss of sea ice concentration (P1 L22, P2 L28, P2 L30). It is the set of loading vectors in (2) that we are concerned with. For example, Fig. R2 above shows the time-averaged patterns of  $\{B_n(r, t), Z_n(r, t), U_n(r, t), \dots\}$  for the first CSEOF mode (sea ice loss mode). It shows how each variable behaves in accordance with the sea ice reduction in the Barents-Kara Seas. Another example is Fig. R3 above, where daily variation of
- 10 each variable averaged over the region of sea ice reduction (red box in Fig. R1a). Based on this figure, we can understand how physical variables respond to the sea ice reduction over the Barents-Kara Seas, and in what way two or more variables

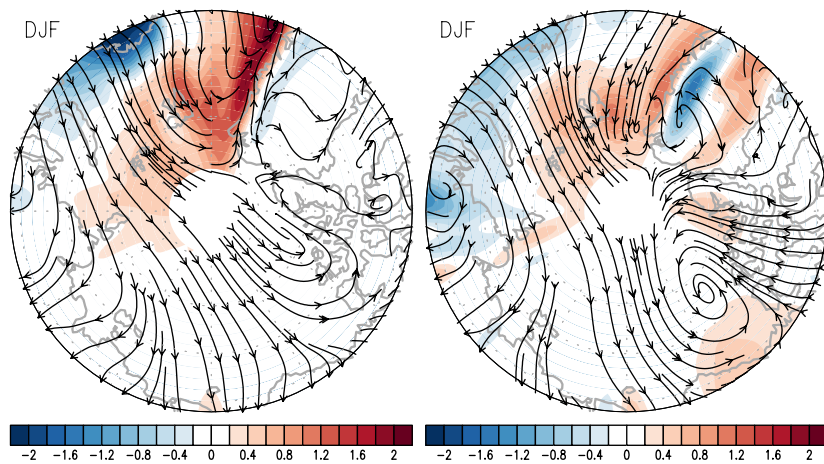
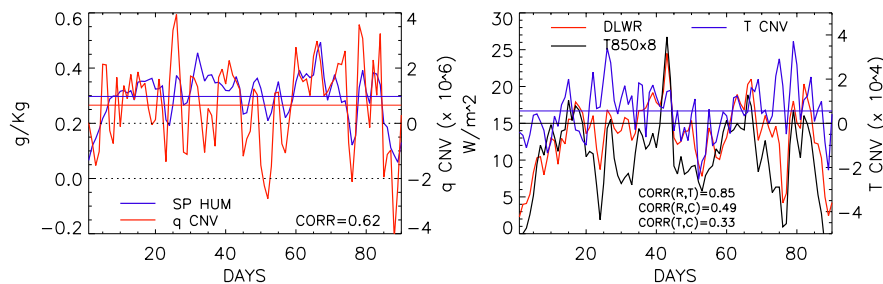


Figure R4. Winter-averaged (left panel) moisture transport (streamline) and its convergence (shade) and (right panel) heat transport (streamline) and its convergence (shade) in the lower troposphere (1000-850 hPa) associated with the sea ice loss mode.

are physically related with each other. As can be seen in Fig. R3, several variables evolve in a very similar manner over the region of sea ice reduction. It also shows how much the winter mean of each variable changes due to sea ice reduction. We do not know how correlation analysis could be used to make the physical inferences similar to those found in the present study.

As the reviewer mentioned, there are other processes such as warm advection that may be important for Arctic amplification and sea ice reduction. As can be seen in Fig. R4, there is a net convergence of moisture transport and heat transport over a region of sea ice reduction, although the center of action is over the Greenland Sea. Thus, moisture and heat transport from lower latitudes apparently affects the variation of sea ice concentration. Figure R5 further shows that there is appreciable correlation between the variation of specific humidity and convergence of moisture transport (corr=0.62) and between the variation of lower tropospheric temperature and convergence of heat transport (corr=0.33). Thus, it seems that both the convergence of moisture transport and the convergence of heat transport are responsible for the variation of specific humidity and temperature in the lower troposphere. On the other hand, the convergence of horizontal transport of moisture cannot explain one essential element of the specific humidity anomaly—the mean of the anomalous specific humidity. As can be seen in Figure R5a, the mean of moisture convergence is close to  $0.6 \times 10^{-6}$  g/kg/sec, which amounts to  $\sim 0.05$  g/kg of

moisture. This value explains only about 17% of the mean value of anomalous specific humidity (~0.3 g/kg); the remainder should derive from a vertical process.



5

Figure R5. The daily time series of anomalous specific humidity and anomalous moisture convergence averaged over the sea ice loss region (21°-79.5°E × 75°-79.5°N) in the Barents-Kara Seas. This particular time series is derived from the regressed loading vectors associated with the sea ice loss mode.

10 Consider the following moisture conservation equation:

$$\frac{\partial q}{\partial t} = -\vec{u} \cdot \nabla q + S \doteq -\nabla \cdot (q\vec{u}) + S = -\nabla_h \cdot (q\vec{u}) - \frac{\partial(qw)}{\partial z} + S. \quad (3)$$

According to Fig. R5, the convergence of the horizontal moisture transport is not so effective as the convergence of the vertical moisture transport in the equation above in terms of increasing the mean of specific humidity. A positive convergence is offset by a negative convergence and vice versa, resulting in a small net increase in the mean of specific humidity. As can be seen in Fig. R6, the anomalous evaporation due to sea ice reduction is positive throughout the winter and its magnitude is reasonable in comparison with the increase in specific humidity. The two time series in Fig. R6 are negatively correlated (except for the mean), indicating that increased (decreased) specific humidity due to positive (negative) convergence of moisture transport reduces (augments) evaporation from the surface of the ocean; this is a reasonable explanation according to the bulk formula.

15

20 Likewise, the variation of the thermal advection and the subsequent convergence of the heat flux are highly correlated with the variation of downward longwave radiation and the lower tropospheric (850 hPa) temperature (see Fig. R5b). On the other hand, the small mean value of the convergence of the horizontal heat flux cannot explain the significant nonzero mean of the anomalous downward longwave radiation or the anomalous lower tropospheric (850 hPa) temperature. Thus, we

25 conclude that the vertical process should be invoked in order to account for the significant changes in the means of the

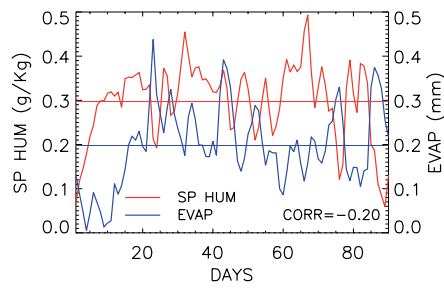


Figure R6. The daily variation of specific humidity (red) and evaporation (blue) averaged over the region of sea ice reduction ( $21^{\circ}$ - $79.5^{\circ}$ E  $\times$   $75^{\circ}$ - $79.5^{\circ}$ N) in the Barents-Kara Seas.

5

variables over the Barents-Kara Seas. We did not simply ignore the contributions of moisture transport and heat transport from lower latitudes. Rather, this is a serious issue and requires more detailed calculation and convincing demonstration, which we considered beyond the scope of the present paper. We, however, acknowledge that we restricted ourselves to processes acting in the Arctic, ignoring the forcing from lower latitudes. Based on this discussion we made the following changes: [P3 L4-5: It should be noted that our discussion is restricted to processes in the Arctic; forcing from lower latitudes can also be important in the process of Arctic amplification and sea ice reduction.]

10

C4: I further do not see any justification for fitting an exponential to the time series of sea ice loss in the Barents-Kara seas, and far less for using that fit to make a prediction on when this ocean area would remain ice-free in winter.

15

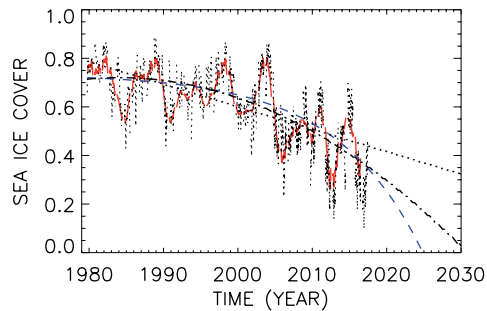


Figure R7. Actual sea ice change in the sea-ice loss region ( $21^{\circ}$ - $79.5^{\circ}$ E,  $75^{\circ}$ - $79.5^{\circ}$ N) of the Barents and Kara Seas (black dotted curve), sea ice change according to the sea ice loss mode (red curve), projections based on the exponential fitting (blue dashed curve), quadratic fitting (dash-dot curve), and linear fitting (dotted curve) of the PC time series.

R4: As can be seen in Fig. 1h in the manuscript, the exponential fitting looks reasonable in describing the change in sea ice concentration in the Barents-Kara Seas. One can use a linear or quadratic fit to make a similar prediction (see Fig. R7). Predictions are predictions whether it is based on the exponential fitting or the fitting of a low order polynomial; uncertainty is inherent in a prediction. We added the predictions based on linear fit and quadratic fit as supplementary information for the benefit of the readers. The reason why we chose the exponential fit (not on the sea ice concentration but on the PC time series of the sea ice loss mode in Fig. 1g in the manuscript) is that it yields the least residual error. The residual error based on a quadratic fit is similar to that of the exponential fit whereas a linear fit yields the largest residual variance among the three. We included some of this discussion and Fig. R7 as supplementary information. We also modified the text as follows:

5 [P1 L24: ... sea ice will completely disappear in the Barents and Kara Seas by as early as 2025, although a conservative  
10 linear fit delays it until 2065.] [P7 L31: We fitted an exponential curve to the amplitude time series of the sea ice loss mode (Fig. 1g); an exponential fitting is chosen, since it minimizes the residual error. Our calculation shows that sea ice in the sea-ice loss region (21°–79.5°E, 75°–79.5 °N) of the Barents and Kara Seas may completely melt by as early as 2025 (Fig. 1h) unless impeded by other naturally occurring variability. A quadratic fit results in a similar result (2030 instead of 2025). A linear fit, the most conservative of the three but with the largest residual error, predicts a complete disappearance of sea ice  
15 in this area by 2065 (see Fig. S4).] We also updated the sea ice concentration curve using the 2017 sea ice data (see new Fig. 1h).

C5: In conclusion, I regret to say that the manuscript fails to meet basic scientific standards.

20 R5: We have addressed all specific comments and are not sure what standards we have failed to meet. We would be happy to address those if they would be identified.

# Understanding the Mechanism of Arctic Amplification and Sea Ice Loss

Kwang-Yul Kim<sup>1</sup>, Jinju Kim<sup>1</sup>, Saerim Yeo<sup>2</sup>, Hanna Na<sup>3</sup>, Benjamin D. Hamlington<sup>4</sup>, and Robert R. Leben<sup>5</sup>

<sup>1</sup>School of Earth and Environmental Sciences, Seoul National University, 1 Gwanak-ro, Gwanak-gu, Seoul 08826, Republic of Korea

<sup>2</sup>APEC Climate Center 1463, Haeundae-gu, Busan 48058, Republic of Korea

<sup>3</sup>Ocean Circulation and Climate Research Center, Korea Institute of Ocean Science and Technology, Ansan, 15627, Republic of Korea

<sup>4</sup>Department of Ocean, Earth and Atmospheric Sciences, 4600 Elkhorn Avenue, Room 406, Old Dominion University, Norfolk, Virginia 23529, USA

<sup>5</sup>Colorado Center for Astrodynamics Research, Department of Aerospace Engineering Sciences, ECNT 320, 431 UCB, University of Colorado, Boulder, Colorado 80309-0431, USA

Correspondence to: Kwang-Yul Kim (kwang56@snu.ac.kr)

**Abstract.** Sea ice reduction is accelerating in the Barents and Kara Seas. Several mechanisms are proposed to explain the accelerated loss of polar sea ice, which remains an open question. In the present study, the detailed physical mechanism of sea ice reduction in winter is identified using the daily ERA interim reanalysis data. Downward longwave radiation is an essential element for sea ice reduction, but can only be sustained by excessive upward heat flux from the sea surface exposed to air in the region of sea ice loss. The increased turbulent heat flux is used to increase air temperature and specific humidity in the lower troposphere, which in turn increases downward longwave radiation. This feedback process is clearly observed in the Barents and Kara Seas in the reanalysis data. A quantitative assessment reveals that this feedback process is amplifying at the rate of ~8.9 % every year during 1979-2016. Based on this estimate, sea ice will completely disappear in the Barents and Kara Seas by ~~as early as 2025, although a conservative linear fit delays it until 2065.~~ Availability of excessive heat flux is necessary for the maintenance of this feedback process; a similar mechanism of sea ice loss is expected to take place over the sea-ice covered polar region when sea ice is not fully recovered in winter.

## 1 Introduction

Over the past decades, rapidly enhanced atmospheric warming has been observed in the Arctic (Serreze and Francis, 2006; Bekryaev et al., 2010; IPCC, 2013). The accelerated warming is pronounced in the lower troposphere during the cold season (Serreze et al., 2009; Screen and Simmonds, 2010a; Screen et al., 2013). An accompanying drastic reduction of sea ice (Comiso et al., 2008; Comiso, 2012) has profound implications for global climate changes by affecting energy exchange between ocean and atmosphere (Serreze and Barry, 2011), and is often referred to as a key factor for accelerated warming in the Arctic (Holland and Bitz, 2003; Serreze et al., 2007; Screen and Simmonds, 2010a; Kumar et al., 2010). A particularly

Jinju Kim 7/7/2017 10:18 AM

Deleted: around 2025

Jinju Kim 7/7/2017 9:48 AM

Deleted: .

significant sea ice reduction can be found over the Barents and Kara seas, which potentially influences cold winter extremes over the Eurasian continent (Petoukhov and Semenov, 2010; Overland et al., 2011; Tang et al., 2013; Cohen et al., 2014; Mori et al., 2014; Kim et al., 2014; Kim and Son, 2016). Physically, sea ice loss involves a positive ice-atmosphere feedback, which leads to an enhanced warming signal in the Arctic region. This feature is generally referred to as Arctic amplification (Screen and Simmonds, 2010a; Serreze and Barry, 2011) and is expected to persist for at least the next decade (IPCC, 2013; Koenigk et al., 2013).

Previous studies have proposed the physical mechanisms of Arctic amplification, which involve the effect of atmospheric heat transport (Graversen et al., 2008), oceanic heat transport (Årthun et al., 2012; Chylek et al., 2009; Spielhagen et al., 2011; Onarheim et al., 2015), cloud and water vapor changes (Francis and Hunter, 2007; Schweiger et al., 2008; Park et al., 2015a; Park et al., 2015b), and/or diminishing sea ice cover (Serreze et al., 2009; Screen and Simmonds, 2010a; Kim et al., 2016). The accurate physical process of the Arctic amplification, however, is subject to debate.

Due to the large seasonal variation of insolation, there exists pronounced seasonality in the air-sea interaction process over the Arctic Ocean. During summer, open water readily absorbs solar radiation, which results in increasing heat content in the oceanic mixed layer. This represents the so-called albedo feedback (Deser et al., 2000; Serreze et al., 2009; Screen and Simmonds, 2010a; Deser et al., 2010; Serreze and Barry, 2011), meaning that the Arctic Ocean is efficient in absorbing atmospheric heat during summer. The albedo feedback is also important during the snow and ice melt in spring and early summer even before the appearance of open sea. After sunsets over the Arctic Ocean, the ice-albedo feedback is suppressed and the primary air-sea interaction mechanism becomes oceanic horizontal advection and vertical convection heat (Screen and Simmonds, 2010b). The stored heat in the ocean mixed layer is released back to the colder atmosphere above, which will result in warming of the atmosphere. The decreased insulation effect (Screen and Simmonds, 2010b) due to the loss of sea ice also promotes further sea ice reduction. Thus, heat transfer between the ocean and atmosphere is generally considered as the fundamental mechanism of Arctic amplification, which is pronounced only during the cold season. On the other hand, increased cloud cover and water vapor (Francis and Hunter, 2007; Schweiger et al., 2008; Graversen and Wang, 2009; Park et al., 2015a; Park et al., 2015b) can also contribute to an increase in downward longwave radiation.

Despite the general consensus that heat transfer between the ocean and atmosphere is a crucial element in the physical mechanism of Arctic amplification and sea ice reduction, a quantitative understanding of individual contributions of heat flux components is still controversial. Further, the role of upward and downward longwave radiations in Arctic amplification is vague and not fully understood. Accurately quantifying the contribution of these different mechanisms, therefore, is required for a complete understanding of the Arctic amplification.

In the present study, a quantitative assessment of energy fluxes involved in the Arctic amplification is investigated in relation to the sea ice reduction over the Barents and Kara Seas. This is an extension of the study by Kim et al. (2016) with a specific goal of delineating the feedback mechanism between sea surface and the atmosphere. In particular, we extract a physically meaningful warming/sea ice reduction signal in the Arctic region and investigate how sea ice loss and individual

Jinju Kim 7/7/2017 9:54 AM

Deleted: ; Vihma 2014

Jinju Kim 7/7/2017 9:49 AM

Deleted: heat transport

energy fluxes are linked in a quantitative manner. For this goal, cyclostationary empirical orthogonal function (CSEOF) analysis is carried out on surface and pressure-level variables derived from the ERA interim daily reanalysis data in winter (Dec. 1-Feb. 28,  $d = 90$  days). It should be noted that our discussion is restricted to process in the Arctic; forcing from lower latitudes can also be important in the process of Arctic amplification and sea ice reduction.

## 5 2 Data and Method of Analysis

### 2.1 Data

ECMWF Reanalysis (ERA) interim daily variables are used from 1979-2016 (Dee et al., 2011). Both surface and pressure-level variables during winter (Dec. 1-Feb. 28) are analyzed over the Arctic region (north of  $60^\circ$  N) to understand the detailed physical mechanism of sea ice melting and Arctic amplification.

### 10 2.2 CSEOF analysis and regression analysis in CSEOF space

Analysis tool used for this study is the CSEOF technique (Kim et al., 1996; Kim and North, 1997; Kim et al., 2015). In CSEOF analysis individual physical processes in space-time data are decomposed as:

$$T(r, t) = \sum_n B_n(r, t) T_n(t), \quad B_n(r, t) = B_n(r, t + d), \quad (1)$$

15 | where  $B_n(r, t)$  depicts daily winter evolution of the  $n$ th physical process and  $T_n(t)$  describes how the amplitude of the evolution varies on a longer time scale, and  $r$  and  $t$  denote location and time, respectively. Since the nested period  $d = 90$  days, each loading vector,  $B_n(r, t)$ , consists of 90 spatial patterns which depict evolution of a variable throughout the winter.

20 | These winter evolution patterns,  $B_n(r, t)$ , repeat every winter, but its amplitude varies from one year to another according to the corresponding PC time series. CSEOF loading vectors are mutually orthogonal to each other in space and time and represent distinct physical processes. The principal component (PC) time series,  $T_n(t)$  are uncorrelated with (and are often nearly independent of) each other. Each loading vector depicts a temporal evolution of spatial patterns seen in a physical process (such as El Niño or seasonal cycle), and corresponding PC time series describes a long-term modulation of the amplitude of the physical process. Thus, the CSEOF technique is suitable for extracting and depicting temporal evolution of (nearly independent) physical processes and often yields valuable insight that cannot be attained from single spatial pattern.

25 | In order to make suitable physical interpretation of the analysis results, CSEOF analysis is conducted on a number of key variables. It is, then, extremely important to make CSEOF loading vectors derived from individual variables to be physically consistent with each other. For the purpose of generating physically consistent CSEOF loading vectors, regression analysis is carried out in CSEOF space (Kim et al., 2015). A target variable is chosen such that its major CSEOF modes best depict the physical process under investigation; target variable is sea ice concentration in the present study.

30 | Once CSEOF analysis on the “target” variable is completed as in (1), physically consistent loading vectors of another variable, called the “predictor” variable, are obtained as follows:

Step 1:  $P(r, t) = \sum_n C_n(r, t)P_n(t)$  (CSEOF analysis on a new variable) (2)

Step 2:  $T_n(t) = \sum_{m=1}^M \alpha_m^{(n)} P_m(t)$  (regression on PC time series) (3)

Step 3:  $Z_n(r, t) = \sum_{m=1}^M \alpha_m^{(n)} C_m(r, t)$  (regressed loading vector) (4)

Then, the target and predictor variables can be written as

$$\{T(r, t), P(r, t)\} = \sum_n \{B_n(r, t), Z_n(r, t)\} T_n(t). \quad (5)$$

Namely, the loading vectors of the two variables,  $B_n(r, t)$  and  $Z_n(r, t)$ , share an identical PC time series,  $T_n(t)$ , for each mode. As a result, the evolution of a physical process manifested as  $B_n(r, t)$  and  $Z_n(r, t)$  in two different variables is governed by a single amplitude time series. Otherwise,  $B_n(r, t)$  and  $Z_n(r, t)$  do not represent the same physical process and henceforth are not physically consistent. This process can be repeated for other predictor variables. As a result of regression,

then, entire data can be written in the form

$$Data(r, t) = \sum_n \{B_n(r, t), Z_n(r, t), U_n(r, t), \dots\} T_n(t), \quad (6)$$

where the terms in curly braces denote physically consistent evolutions derived from various physical variables. [A rigorous mathematical explanation of the regression analysis in CSEOF space can be found in Kim et al. \(2015\).](#)

Aside from the winter seasonal cycle, the first CSEOF mode derived from the daily winter sea ice concentration data in the Arctic depicts sea ice loss and associated Arctic warming in the Barents and Kara Seas. [This mode explains 24% of the total variability of the sea ice concentration in the Arctic Ocean and is the focus of investigation in the present study.](#)

### 3 Results and Discussion

Figure 1 shows the winter-averaged pattern of  $B_1(r, t)$  together with the regressed patterns from other variables (the terms in the curly braces in (6)). We refer to it as the sea ice loss mode, since the loading vector (Fig. 1a; see also Fig. 2) and the amplitude time series (Fig. 1g) describes the sea ice reduction, together with natural variability of sea ice concentration, in the Barents and Kara Seas during the past 37 years (Fig. 1h). [The pattern of sea ice reduction \(Fig. 1a\) is nearly identical with the trend pattern of sea ice concentration in the Arctic Ocean \(see Fig. S1 in the supplementary information\). As can be seen in Fig. 1h, the sea ice reduction trend in the Barents and Kara Seas \(boxed area in Fig. 1a\) is faithfully captured by this mode.](#) In particular, the rate of sea ice loss has significantly increased since 2004-2005 (Vihma, 2014). In association with the sea ice reduction, 2 m air temperature, 850 hPa temperature, specific humidity, upward longwave radiation, downward longwave radiation, and upward heat flux have increased significantly over the region of major sea ice reduction ( $21^\circ$ - $79.5^\circ$  E  $\times$   $75^\circ$ - $79.5^\circ$  N) (black boxed area in Fig. 1a). As can be seen in Figs. 1a, 1c and 1e, the central areas of anomalous 2 m air temperature, upward longwave radiation and turbulent (sensible + latent) heat flux match well with the region of sea ice loss (Screen and Simmonds, 2010b). On the other hand, the centers of downward longwave radiation and specific humidity match well with that of the 850 hPa air temperature (Figs. 1b, 1d, and 1f).

[Sea ice concentration varies slightly on a daily basis, and its fluctuation is less than 2% from the mean value of -14.7% throughout the winter \(Fig. 2\).](#) In accordance with the reduced sea ice concentration, upward longwave radiation

Jinju Kim 7/7/2017 9:52 AM  
Formatted: Indent: First line: 1.27 cm

Jinju Kim 7/7/2017 9:57 AM  
**Deleted:** Sea ice concentration varies slightly on a daily basis, and it remains to be nearly stationary throughout the winter (Fig. 2).

flux is increased from the warmer sea surface exposed to air. Multiplying the amplitude (PC) time series (Fig. 1g) with the loading vector (Fig. 2) of the sea ice loss mode as in (1), actual sea ice concentration time series is obtained as in Fig. 1h. According to Fig. 1h, sea ice concentration has decreased by ~40% during the last 37 years.

Figure 3 shows the anomalous surface (2 m) air temperature the lower tropospheric geopotential height and wind and the vertical section of anomalous temperature, geopotential height and wind along 60°E and 80°N associated with sea ice reduction. A significant warming is seen in the lower troposphere (e.g., Serreze and Francis, 2006; Serreze et al., 2007; Screen et al., 2013). Note that the anomalous temperature pattern is similar to the second EOF pattern in Graversen et al. (2008). The anomalous temperature and geopotential height are consistent according to the hydrostatic equation (see Fig. S2). Anomalous wind and geopotential height are consistent according to the thermal wind equation. As can be seen, an anticyclonic circulation is established over the region of sea ice loss. This anticyclonic circulation results in advection of warmer air over the Barents and Kara Seas and advection of colder air over the mid-latitude East Asia (Kim and Son, 2016).

The winter-averaged patterns of anomalous downward longwave radiation and specific humidity look fairly similar to that of 850 hPa air temperature (Figs. 4a and 4b). It appears that the increased downward longwave radiation is the result of the tropospheric warming (Fig. 3). Specific humidity also increases with the tropospheric warming. Note specifically that these changes are observed over or close to the region of sea ice reduction. The patterns of total cloud liquid water and total cloud ice water, which are the key variables for the formation of clouds, also exhibit a strong response over the region of sea ice reduction although their centers of action are shifted toward the Greenland Sea (Fig. 4d). The pattern of total cloud cover, however, does not show any strong cloud activity over the region of sea ice reduction (Fig. S3 in the supplementary information); it should be understood that cloud cover is a difficult variable to simulate accurately in a reanalysis model.

Therefore, we postulate that the increased downward longwave radiation is due to the increased 850 hPa air temperature and the greenhouse effect produced by the increased specific humidity. Further note that net (upward minus downward) longwave radiation is positive over the region of major sea ice reduction, whereas it is slightly negative over the surrounding areas (Fig. 4c). Thus, at the surface level, there is a net loss of longwave energy over the region of sea ice reduction, while there is a net gain of longwave radiation over the surrounding area.

A prominent source of energy available for heating the atmospheric column is the increased turbulent heat flux from the sea surface exposed to air due to sea ice reduction (Fig. 5). Figure 6 shows the winter daily variations of the regressed loading vectors in (6) (terms in curly braces) averaged over the region of sea ice reduction (21°-79.5° E × 75°-79.5° N); it may be interpreted as atmospheric response to the sea ice reduction shown in Fig. 2. Although the total (area-weighted) magnitudes of sensible and latent heat fluxes are generally smaller than those of upward and downward longwave radiation (see Fig. 6a), turbulent heat flux (see Fig. 5) is locally more pronounced than longwave radiations (Deser et al., 2010). Furthermore, the combined effect of turbulent heat flux is about 6 times larger than that of longwave radiation, since upward and downward longwave radiation tends to offset each other and the resulting net longwave radiation is comparatively smaller than the net upward turbulent heat flux (Fig. 6a). In the presence of turbulent heat flux, air temperature and, henceforth, downward longwave radiation can increase continually leading to further sea ice reduction.

Jinju Kim 7/7/2017 9:54 AM

**Deleted:** Judging from the amplitude time series of the sea ice loss mode (Fig. 1h), sea ice concentration has been reduced by ~40% during the last 35 years.

Jinju Kim 7/7/2017 10:21 AM

**Deleted:** and

Jinju Kim 7/7/2017 9:55 AM

**Deleted:** 925 hPa air temperature (upper panels)

Jinju Kim 7/7/2017 9:56 AM

**Deleted:** The pattern of total cloud cover, on the other hand, differs significantly from that of sea ice concentration or downward longwave radiation (Fig. 4d) (Screen and Simmonds, 2010a). The pattern of total cloud cover associated with the sea ice loss mode does not exhibit any strong cloud activity over the region of sea ice reduction, suggesting little connectivity between sea ice reduction and change in cloud cover. It should be understood, however, that cloud cover is a difficult variable to simulate accurately in a reanalysis model.

While the increased downward longwave radiation is a key element of sea ice reduction, it is not a sustainable physical process by itself. The area-averaged magnitudes of the upward and downward longwave radiation exceed those of the sensible and latent heat flux in the Barents and Kara Seas (Fig. 6a). The net amount of upward longwave radiation, however, is much smaller than the net upward heat flux as a result of near cancellation between the upward and downward longwave radiations. In fact, the upward radiation is, in general, slightly larger than the downward radiation resulting in the net upward longwave radiation of  $\sim 2 \text{ W m}^{-2}$  in winter in the Barents and Kara Seas. This implies that surface temperature should decrease, preventing further sea ice reduction. A decrease in surface air temperature also means that tropospheric air temperature should decrease. In this sense, downward longwave radiation alone is not sufficient to sustain the sea ice reduction process. On the other hand, the net amount of heat flux is  $\sim 12 \text{ W m}^{-2}$  in the same area. Once ocean surface is exposed due to the reduction of sea ice by ocean current (Schlichtholz, 2011; Smedsrud et al., 2013) or wind (Park et al., 2015b), the enhanced turbulent heat flux helps sustain sea ice reduction.

As can be seen in Figs. 6b and 6c, daily upward longwave radiation change over the sea ice loss region is highly correlated with the daily fluctuation of 2 m air temperature, whereas daily downward longwave radiation change is strongly correlated with both 850 hPa and 2 m air temperatures. According to the lagged correlations (Fig. 7), daily changes of both upward and downward longwave radiations in the sea ice loss mode are highly correlated with those of 2 m air temperature and 850 hPa air temperature to a lesser extent. According to analysis based on 3-hourly data, 850 hPa air temperature leads changes in downward longwave radiation. Change in 2 m air temperature, on the other hand, is nearly simultaneous with the downward longwave radiation, whereas it slightly leads the upward longwave radiation. It appears that the increased tropospheric temperature increases the downward longwave radiation, which leads to a sea ice reduction. As a result, surface temperature and upward longwave radiation may increase.

Therefore, we propose a feedback mechanism as suggested in Fig. 8. Sea ice reduction in this area leads to an increase in upward heat flux, which is used to raise temperature in the lower troposphere. Warming in the lower troposphere increases downward longwave radiation. As a result, sea ice melts. This feedback process can be written mathematically as follow:

$$\text{Step 1: } \frac{dFL^\uparrow}{dt} = -\alpha \frac{dS}{dt}, \quad FL^\uparrow = SW^\uparrow - SW^\downarrow + LW^\uparrow - LW^\downarrow + SF^\uparrow + LF^\uparrow, \quad (7)$$

$$\text{Step 2: } \frac{dT}{dt} = \beta \frac{dFL^\uparrow}{dt}, \quad (8)$$

$$\text{Step 3: } \frac{dLW^\downarrow}{dt} = \gamma \frac{dT}{dt}, \quad (9)$$

$$\text{Step 4: } \frac{dS}{dt} = -\delta \frac{dLW^\downarrow}{dt}, \quad (10)$$

where  $S$  is sea ice concentration,  $T$  is tropospheric (850 hPa) temperature,  $LW^\downarrow$  is downward longwave radiation, and the net upward flux  $FL^\uparrow$  is the sum of net short and longwave radiations and sensible and latent heat fluxes. According to the winter

Jinju Kim 7/7/2017 9:58 AM

**Deleted:** air

Jinju Kim 7/7/2017 9:58 AM

**Deleted:** . As a result, 2 m air temperature increases and subsequently upward longwave radiation increases. Further, both downward and upward longwave radiation changes seem to lead sea ice concentration change.

Jinju Kim 7/7/2017 9:58 AM

**Deleted:** surface air temperature increases and

(90-day) averaged loading vector of the sea ice loss mode,  $\alpha = 1.016 \times 10^2$ ,  $\beta = 9.522 \times 10^{-2}$ ,  $\gamma = 1.155 \times 10^1$ , and  $\delta = 8.946 \times 10^{-3}$ . It is emphasized that sea ice reduction continues, since downward longwave radiation continues to increase via enhanced upward heat flux from the exposed sea surface. According to our model, 1 % reduction in sea ice coverage leads to  $1.02 \text{ W m}^{-2}$  increase in upward energy flux, which, in turn, leads to 0.09 K increase in 850 hPa air temperature and  $0.91 \text{ W m}^{-2}$  increase in downward longwave radiation.

Note that this feedback mechanism, in its present form, does not require any delayed action of increased absorption of insolation during summer in terms of albedo feedback. In winter, a significant amount of turbulent heat flux can be released from the ocean exposed to cold air without excessive energy stored in summer. Summer heating, on the other hand, may be a fortifying factor for this feedback loop by preventing sea ice from refreezing during fall and winter.

According to the amplitude time series in Fig. 1g, the rate of sea ice melting appears to be accelerating. A curve fit with an exponential function results in

$$pc(t) = a \exp(\lambda t) + b = a(e^\lambda)^t + b \cong a(1 + \lambda)^t + b, \quad (11)$$

where  $pc(t)$  is the amplitude time series in Fig. 1g, and  $t$  is time in years since 1979. We obtained the fitting curve (dashed curve in Fig. 1g) with parameters  $a = 1.275 \times 10^{-1}$ ,  $\lambda = 8.916 \times 10^{-2}$ , and  $b = -9.055 \times 10^{-1}$ . Equation (11) can be rewritten as

$$pc(t) - c = (pc(0) - c)(1 + \lambda)^t. \quad (12)$$

That is, the amplitude of sea ice melting and atmospheric warming increases at the rate of  $\sim 8.9\%$  every year.

#### 4 Concluding Remarks

A quantitative estimation of changes in the sea ice and other key variables in the Barents and Kara Seas reveals that increase in downward longwave radiation is sustained by an increase in turbulent flux from the exposed sea surface. While a wider area of sea surface is exposed to air and upward longwave radiation increases due to summer sea surface warming, the increased upward longwave radiation alone seems insufficient to produce a feedback loop. Due to a net deficit of surface radiation in fall/winter, sea ice may refreeze quickly (see Figs. 7 and 8 in Kim et al., 2016). Prolonged sea ice melting is instrumental for increased turbulent flux, which in turn warms the atmospheric column (see Fig. 5). As a result, downward longwave radiation increases and sea ice reduction continues in accordance with surface warming (Fig. 8). This is why significant Arctic amplification is observed only in the Barents and Kara Seas but not in the Laptev, East Siberian or Chukchi Seas, where summer sea ice melting is conspicuous but sea ice quickly refreezes in late fall/early winter (Kim et al., 2016). How sea ice refreezing is delayed in the Barents and Kara Seas remains to be answered. Sea ice cover in the Barents and Kara Seas was  $\sim 80\%$  in 1979 and is currently  $\sim 40\%$ . We fitted an exponential curve to the amplitude time series of the sea ice loss mode (Fig. 1g): an exponential fitting is chosen, since it minimizes the residual error. Our calculation shows that sea ice in the sea-ice loss region ( $21^\circ\text{--}79.5^\circ\text{E}$ ,  $75^\circ\text{--}79.5^\circ\text{N}$ ) of the Barents and Kara Seas may completely melt by as early as 2025 (Fig. 1h) unless impeded by other naturally occurring variability. A quadratic fit results in a similar result (2030 instead

Jinju Kim 7/7/2017 9:59 AM

**Deleted:** As a result, 2 m air temperature increases by 0.24 K (see Fig. 6).

of 2025). A linear fit, the most conservative of the three but with the largest residual error, predicts a complete disappearance of sea ice in this area by 2065 (see Fig. S4).

It should be pointed out that this feedback process could develop in other areas of the Arctic Ocean. If sea ice refreezing is delayed in late fall/winter, increased turbulent heat flux from the open sea surface will make it more difficult for sea surface to refreeze, ultimately leading to the feedback process in Fig. 8. It is, of course, difficult to determine when this should occur, since environmental factors differ from one location to another. Finally, it should be mentioned that the feedback process does not seem to be sensitive to a choice of the dataset. A similar experiment conducted by using the NCEP reanalysis data produces essentially identical results except for a slight overestimation of the strength of the anomalous patterns in Fig. 1a-f and Fig. 6 (see Figs. S5 and S6 in the supplementary information).

## 10 5 Data and code availability

All the results of analysis and the programs used in the present paper are freely available by contacting the corresponding author.

*Acknowledgments.* This research was supported by the National Science Foundation of Korea under the grant number NRF-2017R1A2B4003930.

Jinju Kim 7/7/2017 10:00 AM

**Deleted:** Our calculation shows that sea ice in the sea-ice loss region (21°-79.5° E × 75°-79.5° N) of the Barents and Kara Seas may completely melt by around 2025 (Fig. 1h) unless impeded by other naturally occurring variability. -

Jinju Kim 7/7/2017 10:00 AM

**Deleted:**

Jinju Kim 7/7/2017 10:00 AM

**Deleted:**

## References

- Árthun, M., Eldevik, T., Smedsrud, L. H., Skagseth, Ø., and Ingvaldsen, R. B.: Quantifying the Influence of Atlantic Heat on Barents Sea Ice Variability and Retreat, *J. Climate*, 25, 4736-4743, 2012.
- 5 Bekryaev, R. V., Polyakov, I. V., and Alexeev, V. A.: Role of polar amplification in long-term surface air temperature variation and modern Arctic warming, *J. Climate*, 23, 3888-3906, 2010.
- Chylek, P., Folland, C. K., Lesins, G., Dubey, M. K., and Wang, M.: Arctic air temperature change amplification and the Atlantic multidecadal oscillation, *Geophys. Res. Lett.*, 36, L14801, doi: 10.1029/2009GL038777, 2009
- Cohen, J., Screen, J. A., Furtado, J. C., Barlow, M., Whittleston, D., Coumou, D., Francis J., Dethloff, K., Entekhabi, D., Overland, J., and Jones, J.: Recent Arctic amplification and extreme mid-latitude weather. *Nat. Geosci.*, 7, 627-637, 10  
2014.
- Comiso, J. C.: Large Decadal Decline of the Arctic Multiyear Ice Cover, *J. Climate* 25, 1176–93, 2012.
- Comiso, J. C., Parkinson C. L., Gersten R., and Stock L.: Accelerated decline in the Arctic sea ice cover, *Geophys. Res. Lett.* 35, L01703, doi:10.1029/2007GL031972, 2008.
- 15 Dee, D., Uppala, S., Simmons, A., Berrisford, P., Poli, P., Kobayashi, S., Andrae, U., Balmaseda, M., Balsamo, G., Bauer, P., Bechtold, P., Beljaars, A. C. M., van de Berg, L., Bidlot, J., Bormann, N., Delsol, C., Dragani, R., Fuentes, M., Geer, A. J., Haimberger, L., Healy, S. B., Hersbach, H., Hólm, E. V., Isaksen, L., Kållberg, P., Köhler, M., Matricardi, M., McNally, A. P., Monge-Sanz, B. M., Morcrette, J. J., Park, B. K., Peubey, C., de Rosnay, P., Tavolato, C., Thépaut, J. N., and Vitart, F.: The ERA-Interim reanalysis: Configuration and performance of the data assimilation system, *Q. J. Roy. Meteor. Soc.*, 137, 553–597, 2011
- 20 Deser, C., Walsh, J. E., and Timlin, M. S.: Arctic sea ice variability in the context of recent atmospheric circulation trends, *J. Climate*, 13, 617-633, 2000.
- Deser, C., Tomas, R., Alexander, M., and Lawrence, D.: The Seasonal Atmospheric Response to Projected Arctic Sea Ice Loss in the Late Twenty-First Century, *J. Climate*, 23, 333-351, 2010.
- Francis, J. A. and Hunter, E.: Changes in the fabric of the Arctic's greenhouse blanket, *Environ. Res. Lett.*, 2, 045011, 25  
doi:10.1088/1748-9326/2/4/045011, 2007.
- Graversen, R. G. and Wang, M.: Polar amplification in a coupled climate model with locked albedo, *Clim. Dynam.*, 33, 629-643, 2009.
- Graversen, R. G., Mauritsen, T., Tjernström, M., Källén, E., and Svensson, G.: Vertical structure of recent Arctic warming, *Nature*, 451, 53-56, 2008.
- 30 Holland, M. M. and Bitz, C. M.: Polar amplification of climate change in coupled models, *Clim. Dynam.*, 21, 221-232, 2003.
- IPCC, Climate change 2013: The physical science basis. Contribution of Working Group I to the Fifth Assessment Report of the Intergovernmental Panel on Climate Change, edited by: Stocker, T.F., Qin, D., Plattner, G.-K., Tignor, M.,

- Allen, S.K., Boschung, J., Nauels, A., Xia, Y., Bex, V., and Midgley, P. M., Cambridge University Press, Cambridge, United Kingdom and New York, NY, USA, 2013.
- Kim, B.-M., Son, S.-W., Min, S.-K., Jeong, J.-H., Kim, S.-J., Zhang, X., Shim, T., and Yoon, J.-H.: Weakening of the stratospheric polar vortex by Arctic sea-ice loss, *Nat. Commun.*, 5, doi:10.1038/ncomms5646, 2014.
- 5 Kim, K.-Y. and North, G. R.: EOFs of harmonizable cyclostationary processes, *J. Atmos. Sci.*, 54, 2416-2427, 1997.
- Kim, K.-Y. and Son, S.-W.: Physical characteristics of Eurasian winter temperature variability, *Environ. Res. Lett.*, 11, 044009, 2016.
- Kim, K.-Y., North, G. R., and Huang, J.: EOFs of one-dimensional cyclostationary time series: Computations, examples, and stochastic modeling, *J. Atmos. Sci.*, 53, 1007-1017, 1996.
- 10 Kim, K.-Y., Hamlington, B. D., and Na, H.: Theoretical foundation of cyclostationary EOF analysis for geophysical and climatic variables: Concepts and examples, *Earth-Sci. Rev.*, 150, 201-218, doi:10.1016/j.earscirev.2015.06.003, 2015.
- Kim, K.-Y., Hamlington, B. D., Na, H., and Kim, J.: Mechanism of seasonal Arctic sea ice evolution and Arctic amplification, *The Cryosphere*, 10, 2191-2202, doi:10.5194/tc-10-2191-2016, 2016.
- 15 Koenigk, T., Brodeau, L., Graverson, R. G., Karlsson, J., Svensson, G., Tjernström, M., Willén, U., and Wyser, K.: Arctic climate change in 21st century CMIP5 simulations with EC-Earth, *Clim. Dynam.*, 40, 2719-2743, 2013.
- Kumar, A., Perlwitz, J., Eischeid, J., Quan, X., Xu, T., Zhang, T., Hoerling, M., Jha, B., and Wang, W.: Contribution of sea ice loss to Arctic amplification, *Geophys. Res. Lett.*, 37, L21701, doi: 10.1029/2010GL045022, 2010.
- Mori, M., Watanabe, M., Shiogama, H., Inoue, J., and Kimoto, M.: Robust Arctic sea-ice influence on the frequent Eurasian cold winters in past decades, *Nat. Geosci.*, 7, 869-873, 2014.
- 20 Onarheim, I. H., Eldevik, T., Áρθun, M., Ingvaldsen, R. B., and Smedsrud, L. H.: Skillful prediction of Barents Sea ice cover, *Geophys. Res. Lett.*, 42, 5364-5371, 2015.
- Overland, J. E., Wood, K. R., and Wang, M.: Warm Arctic-cold continents: climate impacts of the newly open Arctic Sea, *Polar Res.*, 30, 15787, 2011.
- 25 Park, D.-S., Lee, S., and Feldstein, S. B.: Attribution of the recent winter sea ice decline over the Atlantic sector of the Arctic Ocean, *J. Climate*, 28, 4027-4033, 2015a.
- Park, H.-S., Lee, S., Son, S.-W., Feldstein, S. B., and Kosaka, Y.: The impact of poleward moisture and sensible heat flux on Arctic winter sea ice variability, *J. Climate*, 28, 5030-5040, 2015b.
- Petoukhov, V. and Semenov, V.: A link between reduced Barents-Kara sea ice and cold winter extremes over northern continents, *J. Geophys. Res.*, 115, D21111, doi:10.1029/2009jd013568, 2010.
- 30 Schlichtholz, P.: Influence of oceanic heat variability on sea ice anomalies in the Nordic Seas, *Geophys. Res. Lett.*, 38, L05705, doi:10.1029/2010GL045894, 2011.
- Schweiger, A. J., Lindsay, R. W., Vavrus, S., and Francis, J. A.: Relationships between Arctic sea ice and clouds during autumn, *J. Climate*, 21, 4799-4810, 2008

- Screen, J. A. and Simmonds, I.: The central role of diminishing sea ice in recent Arctic temperature amplification, *Nature*, 464, 1334-1337, doi:10.1038/nature09051, 2010a.
- Screen, J. A. and Simmonds, I.: Increasing fall-winter energy loss from the Arctic Ocean and its role in Arctic temperature amplification, *Geophys. Res. Lett.*, 37, L16707, doi:10.1029/2010GL044136, 2010b
- 5 Screen, J. A., Simmonds, I., Deser, C., and Tomas, R.: The atmospheric response to three decades of observed Arctic sea ice loss, *J. Climate*, 26,1230-1248, 2013.
- Serreze, M. C. and Barry, R. G.: Processes and impacts of Arctic amplification: A research synthesis, *Global Planet Change*, 77, 85-96, 2011.
- Serreze, M. C. and Francis, J. A.: The Arctic amplification debate, *Climatic Change*, 76, 241-264, 2006.
- 10 Serreze, M. C., Holland, M. M., and Stroeve, J.: Perspectives on the Arctic's Shrinking Sea-Ice Cover, *Science*, 315, 1533-1536, 2007.
- Serreze, M. C., Barrett, A. P., Stroeve, J. C., Kindig, D. N., and Holland, M. M.: The emergence of surface-based Arctic amplification, *The Cryosphere*, 3, 11-19, 2009.
- Smedsrud, L. H., Easun, I., Ingvaldsen, R. B., Eldevik, T., Haugan, P. M., Li, C., Lien, V. S., Olsen, A., Omar, A. M., Otterå, O. H., Risebrobakken, B., Sandø, A. B., Semenov, V. A., and Sorokina, S. V.: The role of the Barents Sea in the Arctic climate system, *Rev. Geophys.*, 15, 415-449, 2013.
- 15 Spielhagen, R. F., Werner, K., Sørensen, S. A., Zamelczyk, K., Kandiano, E., Budeus, G., Husum, K., Marchitto, T. M., and Hald, M.: Enhanced Modern Heat Transfer to the Arctic by Warm Atlantic Water, *Science*, 331, 450-453, 2011.
- Tang, Q., Zhang, X., Yang, X., and Francis, J. A.: Cold winter extremes in northern continents linked to Arctic sea ice loss, *Environ. Res. Lett.*, 8, 014036, doi:10.1088/1748-9326/8/1/014036, 2013.
- 20 Vihma, T.: Effects of Arctic sea ice decline on weather and climate: a review, *Surv. Geophys.*, 35, 1175-1214, 2014.

## Figure Captions

**Figure 1.** Winter (Dec. 1-Feb. 28) average patterns of sea ice loss mode: (a) sea ice (shading) and 2 m air temperature (contour), (b) 1000-850 hPa specific humidity, (c) upward longwave radiation, (d) downward longwave radiation, (e) turbulent (sensible + latent) heat flux, (f) 850 hPa air temperature, (g) the corresponding amplitude change (red solid curve) and the amplification curve (blue dashed curve), and (h) actual sea ice change in the sea-ice loss region ( $21^{\circ}$ - $79.5^{\circ}$  E  $\times$   $75^{\circ}$ - $79.5^{\circ}$  N; the boxed area in (a) of the Barents and Kara Seas (black dotted curve; extended until 2017 based on new data), sea ice change according to the sea ice loss mode (red curve), projection based on the amplification curve (blue dashed curve). The red curve in Fig. 1h is obtained by multiplying the loading vector of sea ice concentration (Fig. 1a) averaged in the boxed area with the amplitude time series (Fig. 1g) according to (1). The green contours in (b)-(f) represent sea ice concentration in (a). The numbers in parenthesis are contour intervals and negative contours are dashed.

**Figure 2.** Anomalous daily sea ice concentration (blue) and upward longwave radiation averaged over the region of sea ice loss ( $21^{\circ}$ - $79.5^{\circ}$  E  $\times$   $75^{\circ}$ - $79.5^{\circ}$  N) with respective mean values (straight lines). Winter days are counted from December 1.

**Figure 3.** Winter-averaged patterns of anomalous atmospheric condition: (a) 2m air temperature, (b) lower tropospheric (1000-900 hPa) geopotential height and wind, (c) vertical cross section along  $60^{\circ}$  E of lower tropospheric (1000-850 hPa) air temperature, geopotential height and wind, and (d) along  $80^{\circ}$ N. Contour intervals are in parenthesis in (a) and (b). Temperature is in shading (0.4 K), geopotential height is in black contours (3 m), and (c) zonal and (d) meridional winds are in blue contours ( $0.2 \text{ m s}^{-1}$ ).

**Figure 4.** Winter-averaged patterns of (a) 850 hPa air temperature (shading) and 2 m air temperature (contour), (b) 900-hPa specific humidity (shade) and downward longwave radiation at surface (contour), (c) net (upward minus downward) longwave radiation at surface (shade) and SAT (contour), and (d) total cloud liquid water (shade) and total cloud ice water (contour) for the sea ice loss mode. The red contour is drawn at the value of the contour interval. The green contours in (a)-(d) represent the reduction of sea ice concentration.

**Figure 5.** Winter average pattern of sea ice loss mode in the Barents and Kara Seas: (a) sea ice (%), shading), 2 m air temperature (red contour) and 850 hPa temperature (black contour), (b) upward longwave radiation (red contour) and downward longwave radiation (black contour), (c) sensible heat flux (red contour) and latent heat flux (black contour), and (d) net energy balance (sensible heat flux + latent heat flux + upward longwave radiation - downward longwave radiation).

**Figure 6.** Daily patterns of variability over the region of sea ice loss ( $21^{\circ}$ - $79.5^{\circ}$  E  $\times$   $75^{\circ}$ - $79.5^{\circ}$  N): (a) upward longwave radiation (blue dashed), downward longwave radiation (blue dotted), net longwave radiation (blue solid) with its mean value (blue straight line), sensible heat flux (red dashed), latent heat flux (red dotted), and turbulent heat flux (red solid) with its mean value (red straight line), (b) 2 m air temperature (red), 850 hPa air temperature  $\times$  2 (black), and upward longwave radiation (blue), and (c) same as (b) except for the regressed downward longwave radiation (blue). The straight lines in (b) and (c) represent the winter mean value of anomalous 2 m air temperature. Correlation of upward and downward longwave radiations with 2 m air temperature is respectively 0.88 and 0.91, whereas with 850 hPa air temperature is 0.66 and 0.85.

Jinju Kim 7/7/2017 10:25 AM

**Deleted:** and purple

Jinju Kim 7/7/2017 10:01 AM

**Deleted:** (a) Anomalous daily sea ice concentration and (b) upward longwave radiation averaged over the region of sea ice loss ( $21^{\circ}$ - $79.5^{\circ}$  E  $\times$   $75^{\circ}$ - $79.5^{\circ}$  N). Winter days are counted from December 1.

Jinju Kim 7/7/2017 10:02 AM

**Deleted:** 925 hPa air temperature,

Jinju Kim 7/7/2017 10:02 AM

**Deleted:** total cloud cover for the sea ice loss mode.

Jinju Kim 7/7/2017 10:24 AM

**Deleted:** and purple

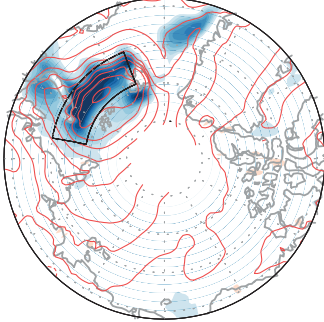
**Figure 7.** Lagged correlations: (a) correlation of upward (solid lines) and downward (dotted lines) longwave radiations with 2 m air temperature (blue), 850 hPa temperature (red), and sea ice concentration (black), and (b) a blow-up of the boxed region in (a). Longwave radiation lags the other variable for a positive lag. Lagged correlation between 2 m air temperature and 850 hPa air temperature (black dashed line); 2 m air temperature leads 850 hPa temperature for a positive lag.

5 **Figure 8.** A proposed mechanism of polar amplification. Increased net upward energy flux increases air temperature. As a result, downward longwave radiation increases, which results in sea ice melting. This loop seems to amplify by ~8.9% annually.

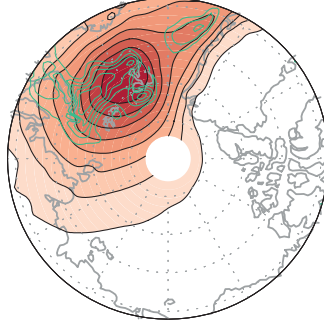
Jinju Kim 7/7/2017 10:03 AM

**Deleted:** warmer surface temperature and

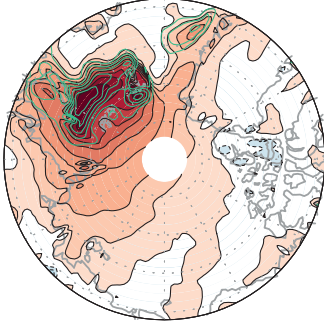
(a) SIC (2%) & 2m AIRT (0.5° C)



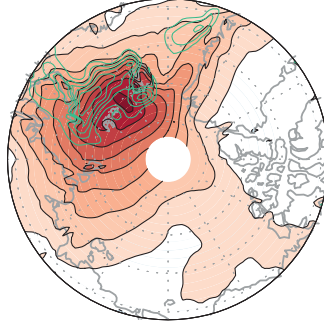
(b) 1000-850 hPa SH ( $3 \times 10^{-2} \text{ g Kg}^{-1}$ )



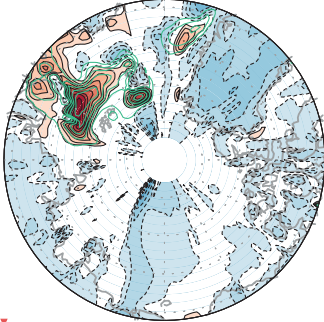
(c) ULW at SFC ( $2 \text{ W m}^{-2}$ )



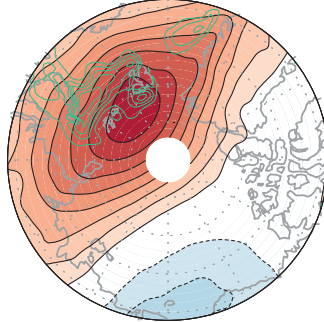
(d) DLW at SFC ( $2 \text{ W m}^{-2}$ )



(e) TURBULENT FLUX ( $4 \text{ W m}^{-2}$ )

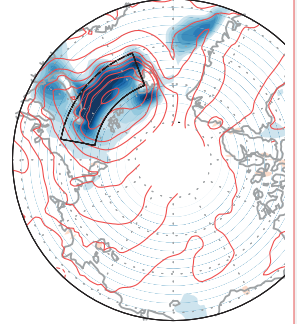


(f) 850 hPa T ( $0.2^\circ \text{ C}$ )

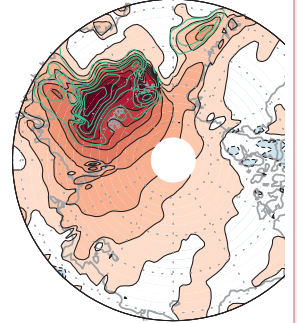


Jinju Kim 7/7/2017 10:07 AM

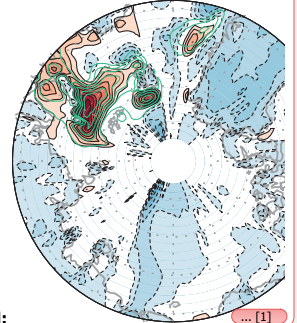
(a) SIC (2%) & 2m AIRT (0.5° C)



(c) ULW at SFC ( $2 \text{ W m}^{-2}$ )

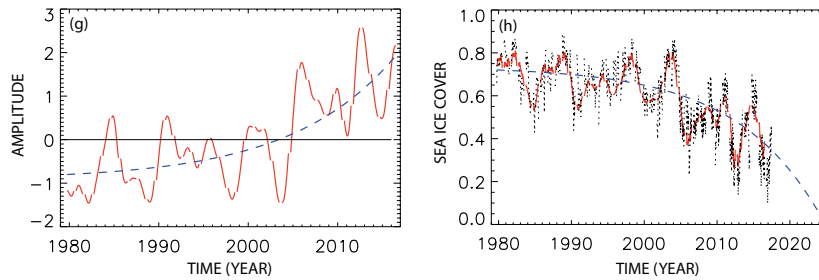


(e) TURBULENT FLUX ( $4 \text{ W m}^{-2}$ )



Deleted:

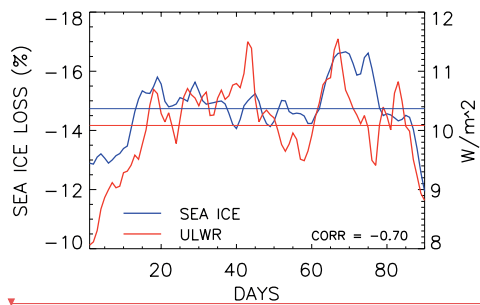
... [1]



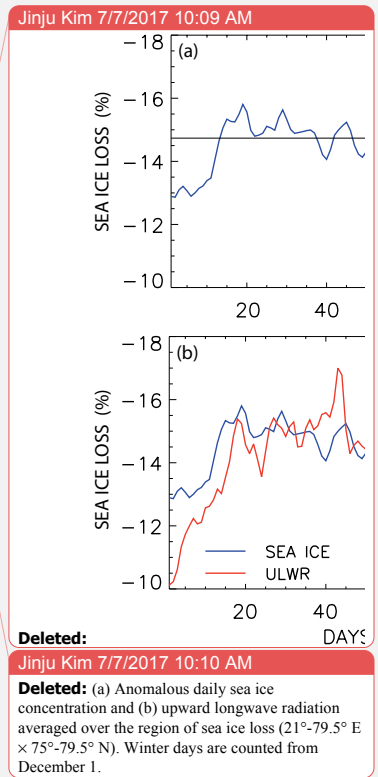
**Figure 1.** Winter (Dec. 1-Feb. 28) average patterns of sea ice loss mode: (a) sea ice (shading) and 2 m air temperature (contour), (b) 1000-850 hPa specific humidity, (c) upward longwave radiation, (d) downward longwave radiation, (e) turbulent (sensible + latent) heat flux, (f) 850 hPa air temperature, (g) the corresponding amplitude change (red solid curve) and the amplification curve (blue dashed curve), and (h) actual sea ice change in the sea-ice loss region ( $21^{\circ}$ – $79.5^{\circ}$  E  $\times$   $75^{\circ}$ – $79.5^{\circ}$  N; the boxed area in (a) of the Barents and Kara Seas (black dotted curve; extended until 2017 based on new data), sea ice change according to the sea ice loss mode (red curve), projection based on the amplification curve (blue dashed curve). The red curve in Fig. 1h is obtained by multiplying the loading vector of sea ice concentration (Fig. 1a) averaged in the boxed area with the amplitude time series (Fig. 1g) according to (1). The green contours in (b)-(f) represent sea ice concentration in (a). The numbers in parenthesis are contour intervals and negative contours are dashed.

Jinju Kim 7/7/2017 10:25 AM

~~Deleted:~~ and purple



**Figure 2.** Anomalous daily sea ice concentration (blue) and upward longwave radiation averaged over the region of sea ice loss ( $21^{\circ}$ - $79.5^{\circ}$  E  $\times$   $75^{\circ}$ - $79.5^{\circ}$  N) with respective mean values (straight lines). Winter days are counted from December 1.



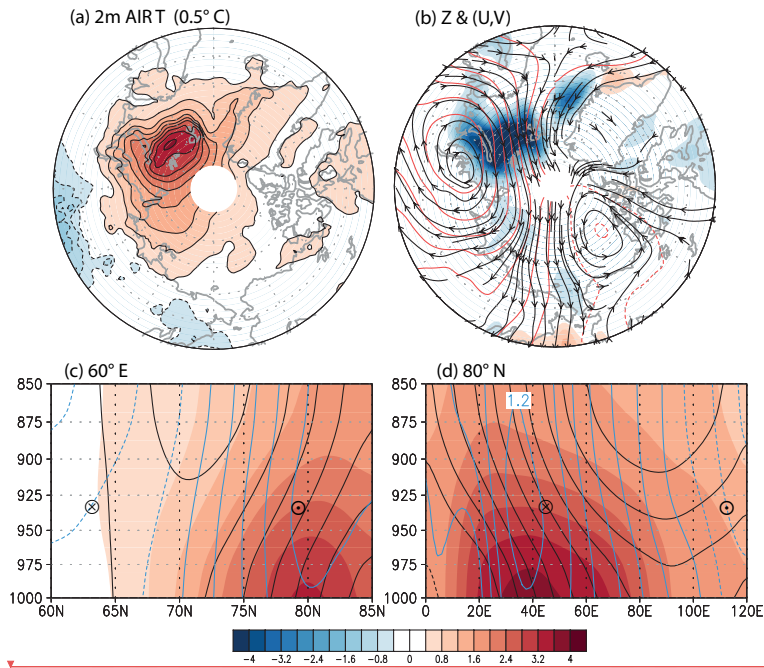
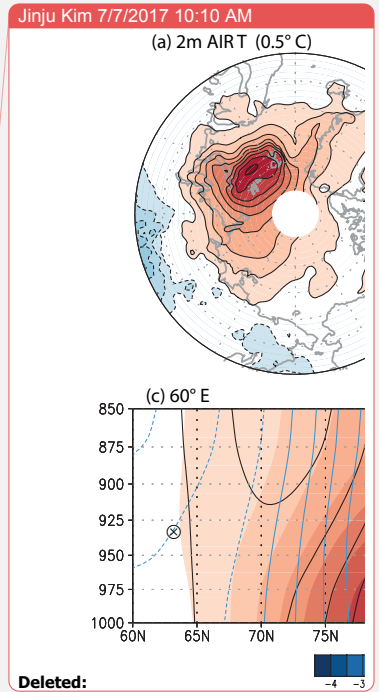
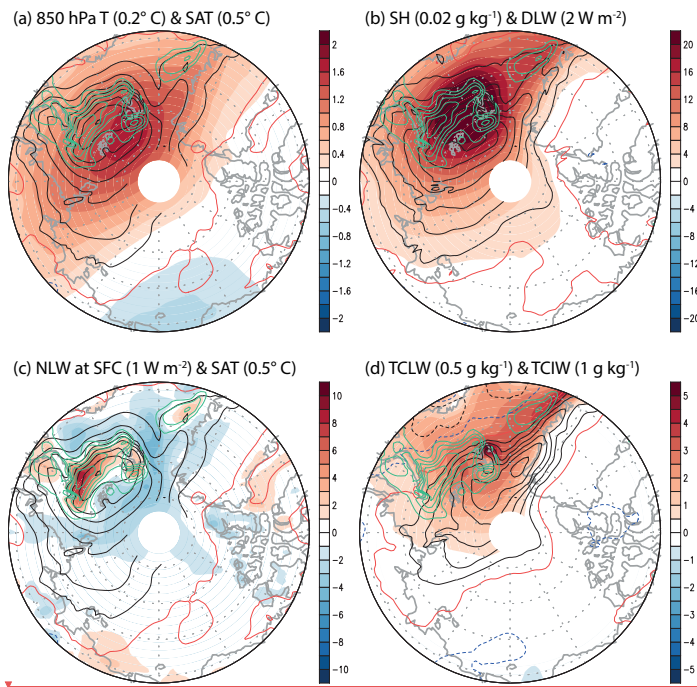


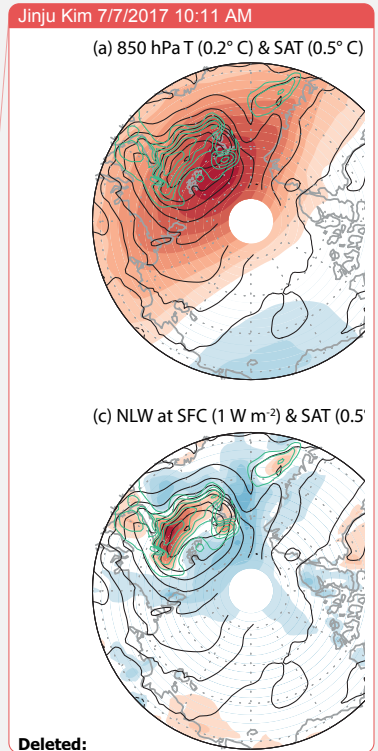
**Figure 3.** Winter-averaged patterns of anomalous atmospheric condition: (a) 2 m air temperature, (b) lower tropospheric (1000-900 hPa) geopotential height and wind, (c) vertical cross section along 60° E of lower tropospheric (1000-850 hPa) air temperature, geopotential height and wind, and (d) along 80° N. Contour intervals are in parenthesis in (a) and (b). Temperature is in shading (0.4 K), geopotential height is in black contours (3 m), and (c) zonal and (d) meridional winds are in blue contours (0.2 m s<sup>-1</sup>).



Jinju Kim 7/7/2017 10:11 AM  
Deleted: 925 hPa air temperature

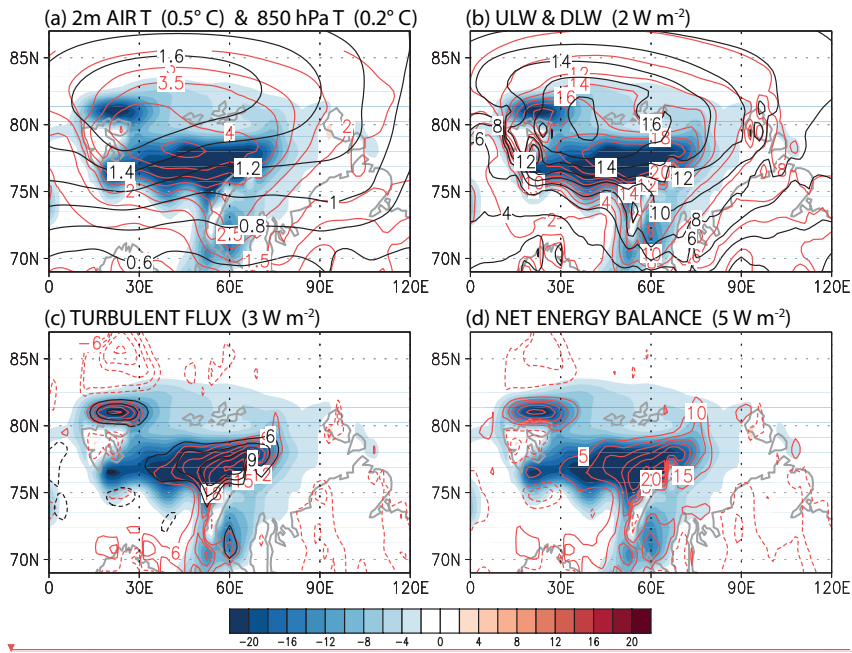


5 **Figure 4.** Winter-averaged patterns of (a) 850 hPa air temperature (shading) and 2 m air temperature (contour), (b) 900-hPa specific humidity (shade) and downward longwave radiation at surface (contour), (c) net (upward minus downward) longwave radiation at surface (shade) and SAT (contour), and (d) total cloud liquid water (shade) and total cloud ice water (contour) for the sea ice loss mode. The red contour is drawn at the value of the contour interval. The green contours in (a)-(d) represent the reduction of sea ice concentration.

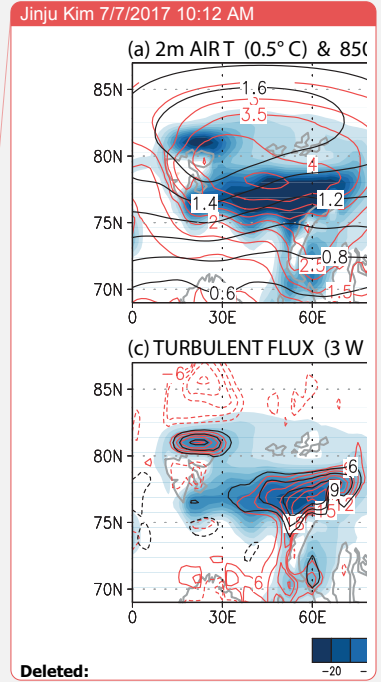


**Deleted:**

Jinju Kim 7/7/2017 10:12 AM  
**Deleted:** total cloud cover for the sea ice loss mode.  
 Jinju Kim 7/7/2017 10:26 AM  
**Deleted:** and purple



5 **Figure 5.** Winter average pattern of sea ice loss mode in the Barents and Kara Seas: (a) sea ice (% , shading), 2 m air temperature (red contour) and 850 hPa temperature (black contour), (b) upward longwave radiation (red contour) and downward longwave radiation (black contour), (c) sensible heat flux (red contour) and latent heat flux (black contour), and (d) net energy balance (sensible heat flux + latent heat flux + upward longwave radiation – downward longwave radiation).



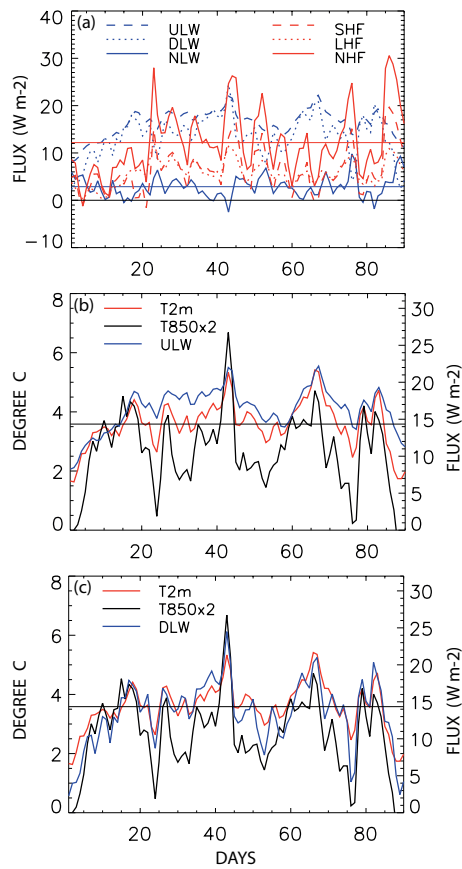
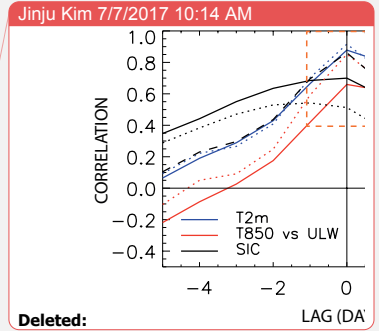
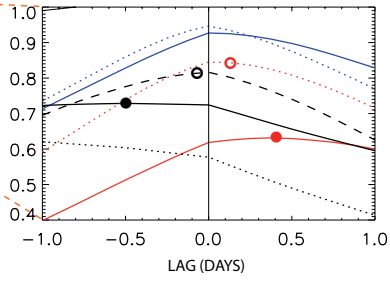
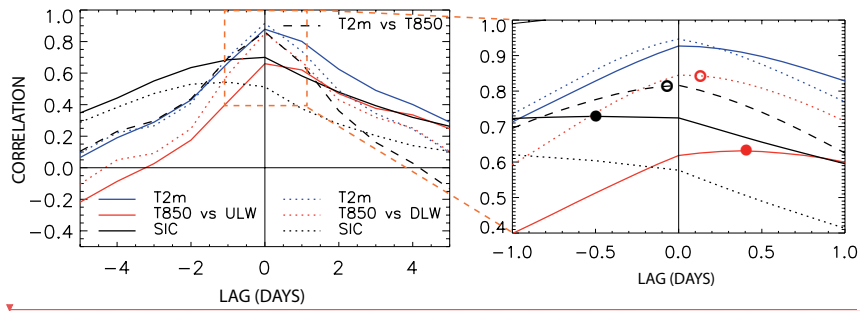


**Figure 6.** Daily patterns of variability over the region of sea ice loss ( $21^{\circ}$ - $79.5^{\circ}$  E  $\times$   $75^{\circ}$ - $79.5^{\circ}$  N): (a) upward longwave radiation (blue dashed), downward longwave radiation (blue dotted), net longwave radiation (blue solid) with its mean value (blue straight line), sensible heat flux (red dashed), latent heat flux (red dotted), and turbulent heat flux (red solid) with its mean value (red straight line), (b) 2 m air temperature (red), 850 hPa air temperature  $\times$  2 (black), and upward longwave radiation (blue), and (c) same as (b) except for the regressed downward longwave radiation (blue). The straight lines in (b) and (c) represent the winter mean value of anomalous 2 m air temperature. Correlation of upward and downward longwave radiations with 2 m air temperature is respectively 0.88 and 0.91, whereas with 850 hPa air temperature is 0.66 and 0.85.

10



5 **Figure 7.** Lagged correlations: (a) correlation of upward (solid lines) and downward (dotted lines) longwave radiations with 2 m air temperature (blue), 850 hPa temperature (red), and sea ice concentration (black), and (b) a blowup of the boxed region in (a). Longwave radiation lags the other variable for a positive lag. Lagged correlation between 2 m air temperature and 850 hPa air temperature (black dashed line); 2 m air temperature leads 850 hPa temperature for a positive lag.

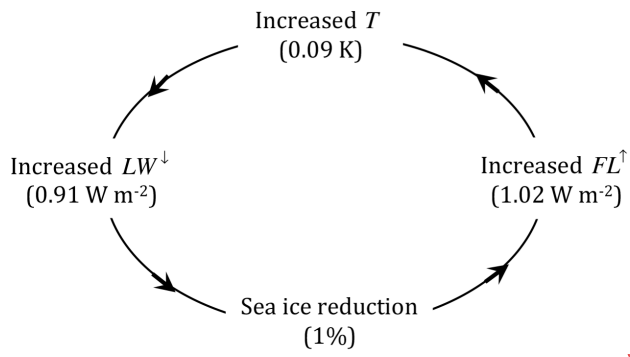


**Figure 8.** A proposed mechanism of polar amplification. Increased net upward energy flux increases air temperature. As a result, downward longwave radiation increases, which results in sea ice melting. This loop seems to amplify by ~8.9 % annually.

Jinju Kim 7/7/2017 10:15 AM

Formatted: Centered

Jinju Kim 7/7/2017 10:15 AM

Deleted: <sp>

Jinju Kim 7/7/2017 10:15 AM

Deleted: in warmer surface temperature

# Supplementary Information

## Understanding the Mechanism of Arctic Amplification and Sea Ice Loss

5 Kwang-Yul Kim<sup>1</sup>, Jinju Kim<sup>1</sup>, Saerim Yeo<sup>2</sup>, Hanna Na<sup>3</sup>, Benjamin D. Hamlington<sup>4</sup>, and Robert R. Leben<sup>5</sup>

<sup>1</sup>School of Earth and Environmental Sciences, Seoul National University, 1 Gwanak-ro, Gwanak-gu, Seoul 08826, Republic of Korea

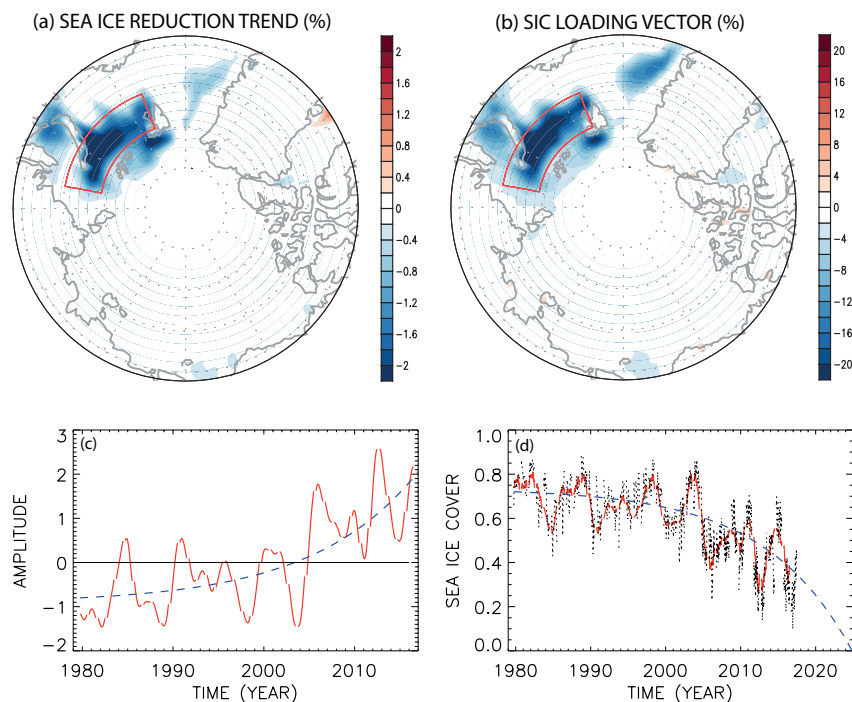
<sup>2</sup>APEC Climate Center 1463, Haeundae-gu, Busan 48058, Republic of Korea

10 <sup>3</sup>Ocean Circulation and Climate Research Center, Korea Institute of Ocean Science and Technology, Ansan, 15627, Republic of Korea

<sup>4</sup>Department of Ocean, Earth and Atmospheric Sciences, 4600 Elkhorn Avenue, Room 406, Old Dominion University, Norfolk, Virginia 23529, USA

<sup>5</sup>Colorado Center for Astrodynamics Research, Department of Aerospace Engineering Sciences, ECNT 320, 431 UCB, University of Colorado, Boulder, Colorado 80309-0431, USA

15 *Correspondence to:* Kwang-Yul Kim (kwang56@snu.ac.kr)



5 **Figure S1.** (a) The yearly trend (%) of sea ice reduction in the Arctic Ocean during 1979-2016, (b) the winter averaged loading vector of the sea ice loss mode, (c) the corresponding PC (amplitude) time series, and (d) actual sea ice concentration in the boxed area (black curve), sea ice concentration according to the sea ice loss mode (red curve) and a projection (red dashed curve) based on the exponential fit of the amplitude time series in (c).

10

Figure S1a is obtained based on a linear trend of sea ice concentration at each grid point based on the ERA-Interim sea ice concentration from 1979-2016. This pattern is nearly identical with the sea ice loss mode discussed in the main text (Fig. S1b). Sea ice reduction is most conspicuous in the Barents-Kara Seas. The amount of sea ice reduction based on the sea ice loss mode is obtained by multiplying the loading vector (Fig. S1b) with its amplitude time series (Fig. S1c), resulting in Fig. S1d. As can be seen in Fig. S1d, the sea ice concentration change due to the sea ice loss mode (red curve) is similar to the actual data (black curve) with a fairly similar rate of trend.

15

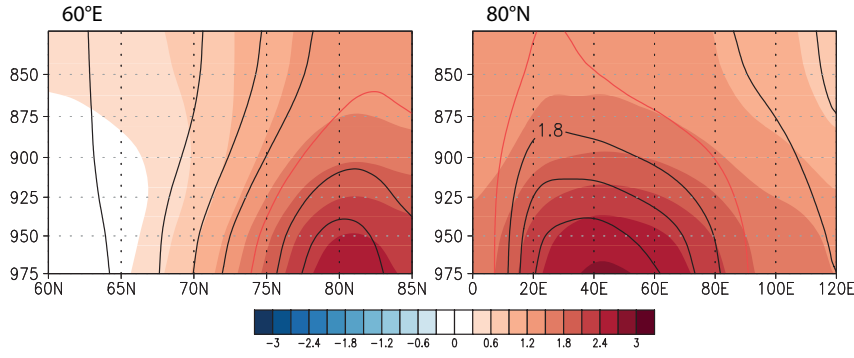


**Figure S2.** The pressure layer thickness ( $\Delta Z = Z(p_1) - Z(p_0)$ ) derived from the geopotential height pattern in Fig. 3 in the text and that derived from the hydrostatic equation (contour). The red contour represents the thickness of 1.5 m. The level  $p_1$  is the level used for plotting and  $p_0$  is the pressure level below  $p_1$  at the interval of 25 hPa.

The shaded geopotential height anomaly in this figure is obtained directly from the geopotential height field in Fig. 3 in the main text, i.e.,

$$(dZ)_j = Z_j - Z_{j-1}, \quad (1)$$

where  $j$  is an index for the vertical level. The contoured geopotential height anomaly is obtained from the temperature field in Fig. 3 in the text, i.e.,

$$(dZ)_j = -\frac{R\langle T \rangle_j}{g} (d \ln p)_j, \quad (2)$$

where

$$(dZ)_j = Z_j - Z_{j-1}, \quad \langle T \rangle_j = (T_j + T_{j-1})/2, \quad (d \ln p)_j = \ln p_j - \ln p_{j-1}. \quad (3)$$

As can be seen in the figure, the anomalous geopotential height field is nearly in hydrostatic balance with the anomalous temperature field. The difference is partially due the use of layer mean temperature  $\langle T \rangle$  in a finite-difference approximation of the hydrostatic equation in (2). Thus, it seems that the release of energy in the form of radiation and heat flux changes the temperature, and geopotential height in the lower troposphere adjusts in accordance with the hydrostatic balance.

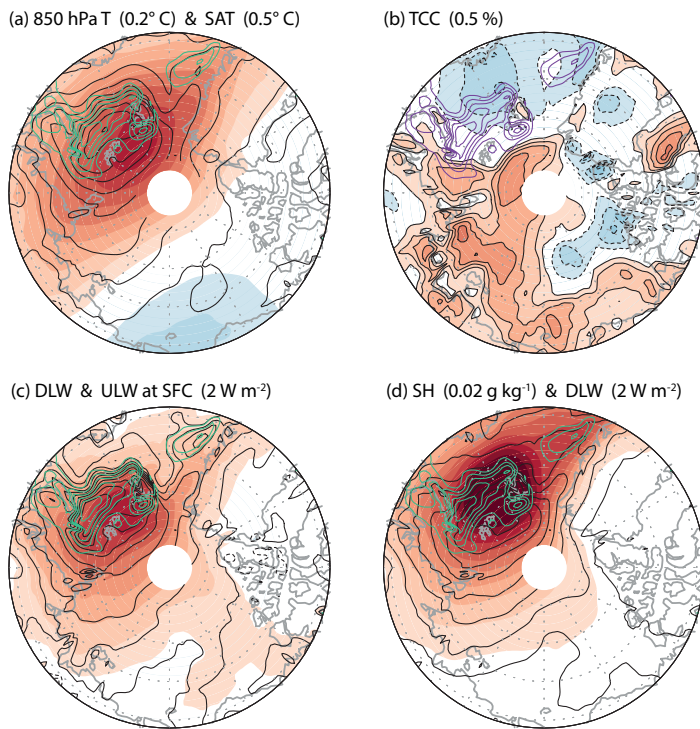


**Figure S3.** The DJF patterns of 850 hPa air temperature (shading) and 2 m air temperature (contour) (a), total cloud cover (b), downward (shade) and upward (contour) longwave radiation at surface (c), and 900-hPa specific humidity (shade) and downward longwave radiation at surface (contour) (d) for the sea ice loss mode. The green and purple contours in (a)-(d) represent the reduction of sea ice concentration.

This figure shows the winter (DJF) averaged patterns of several key variables associated with the sea ice reduction. As can be seen, anomalous patterns of all the variables exhibit strong coherence with that of sea ice reduction except for total cloud cover. The pattern of total cloud cover associated with the sea ice loss mode does not exhibit any strong cloud activity over the region of sea ice reduction, suggesting little connectivity between sea ice reduction and change in cloud cover. However, total cloud liquid water and total cloud ice water, which are two important elements for the production of clouds are reasonably consistent with the pattern of sea ice reduction (see Fig. 4 in the main text).

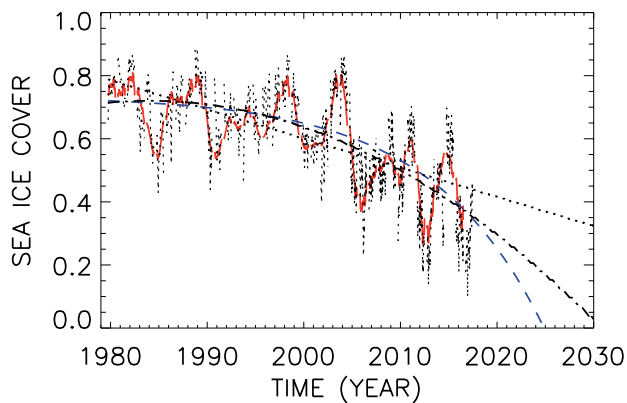


**Figure S4.** Actual sea ice change in the sea-ice loss region ( $21^{\circ}$ – $79.5^{\circ}$ E,  $75^{\circ}$ – $79.5^{\circ}$ N) of the Barents and Kara Seas (black dotted curve; updated until Feb. 2017 using new dataset), sea ice change according to the sea ice loss mode (red curve),  
 5 projections based on the exponential fitting (blue dashed curve), quadratic fitting (dash-dot curve), and linear fitting (dotted curve) of the PC time series.

This figure shows projections of sea ice concentration in the sea-ice loss region of the Barent-Kara Seas based on a linear fit  
 10 (dotted curve), a quadratic fit (dash-dot curve), and an exponential fit (dashed). Residual variance is measured by

$$\varepsilon^2 = \text{var}(S(t) - F(t)),$$

where  $S(t)$  is the sea ice concentration curve (black curve in Fig. S4) and  $F(t)$  is a fit. The exponential fit results in the least  
 residual variance, whereas the linear fit the largest residual variance. The residual variance of the quadratic fit is similar to  
 that of the exponential fit. Sea ice in the region ( $21^{\circ}$ – $79.5^{\circ}$ E,  $75^{\circ}$ – $79.5^{\circ}$ N) disappears completely by 2025 (2030, 2065)  
 15 according to the exponential (quadratic, linear) fit. According to the newly available data, sea ice concentration in this area  
 is the lowest during 2016 winter (Dec. 2016-Feb. 2017; see the dotted line in Fig. S4).

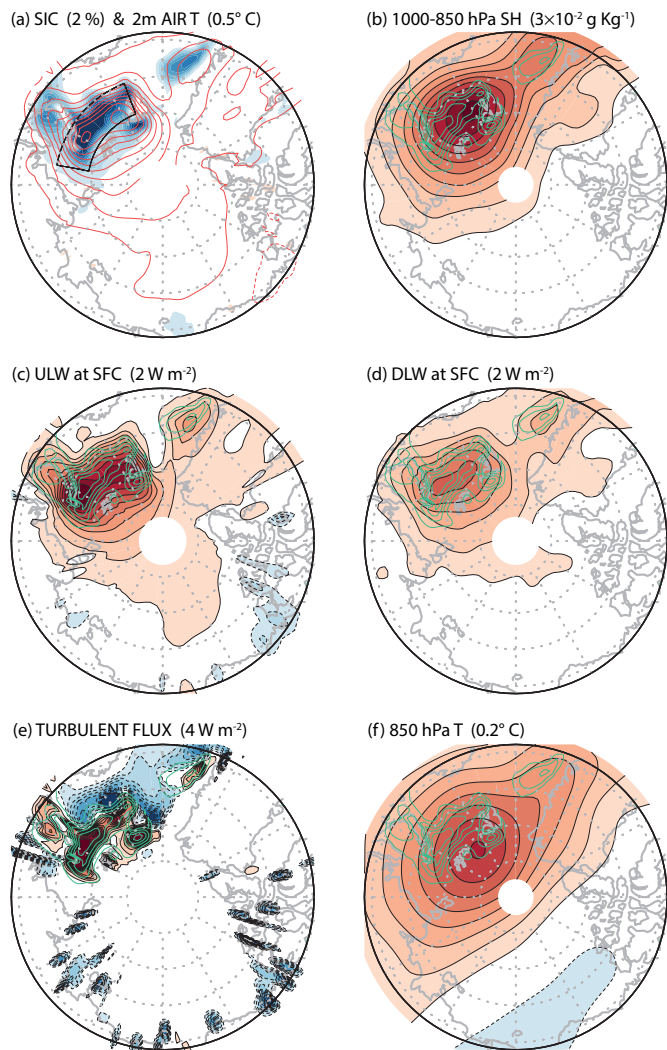


**Figure S5.** Winter (Dec. 1-Feb. 28) average patterns of sea ice loss mode derived from the NCEP reanalysis data: (a) sea ice (shading) and 2 m air temperature (contour), (b) 1000-850 hPa specific humidity, (c) upward longwave radiation, (d) downward longwave radiation, (e) turbulent (sensible + latent) heat flux, (f) 850 hPa air temperature.

This figure shows the winter-averaged patterns of key variables from the NCEP reanalysis product (1979-2016) associated with the sea ice loss mode. The target variable is the ERA-Interim sea ice concentration as in the main text. This figure is fairly similar to Fig. 1a-f in the text except for a small difference in magnitude. Thus, an essentially identical physical process is identified in the NCEP reanalysis product. This result indicates that the physical mechanism addressed in the present study is not overly sensitive to the choice of the dataset for analysis.

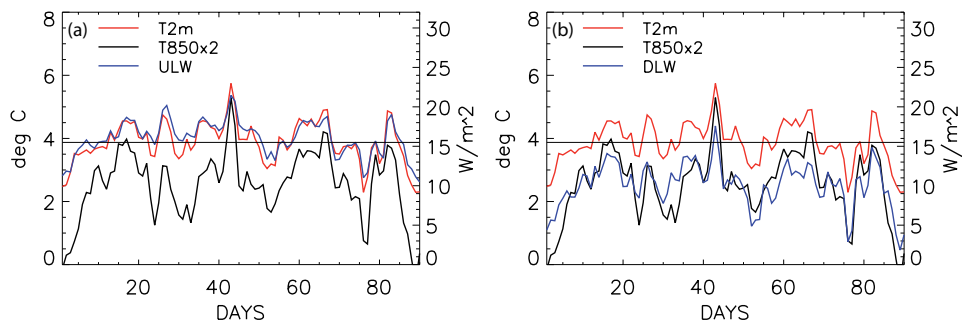


**Figure S6.** Daily pattern of variability over the region of sea ice loss ( $21^{\circ}$ - $79.5^{\circ}$ E  $\times$   $75^{\circ}$ - $79.5^{\circ}$ N) derived from the NCEP reanalysis data: (a) 2 m air temperature (red), 850 hPa air temperature  $\times$  2 (black), and upward longwave radiation (blue), and (b) same as (a) except for the regressed downward longwave radiation (blue). The straight line represents the winter mean value of anomalous 2 m air temperature. Correlation of upward and downward longwave radiation with 2 m air temperature is respectively 0.95 and 0.94, whereas correlation with 850 hPa air temperature is respectively 0.81 and 0.86.

This figure shows the daily evolution of surface (2 m) air temperature, 850 hPa air temperature, upward longwave radiation and downward longwave radiation during winter in response to sea ice reduction in the Barents-Kara Seas as in Fig. 2 in the main text. This result is obtained by using the NCEP reanalysis data. A comparison with Fig. 6 in the main text shows that the response of atmospheric variables to the sea ice reduction in the Barents-Kara Seas as identified from the NCEP reanalysis product is fairly similar to that derived from the ERA-Interim reanalysis product. This figure together with Fig. S4 indicates that the physical process of sea ice reduction and Arctic warming discussed in the text is not sensitive to the choice of analysis dataset.